# CrystEngComm



## **PAPER**

View Article Online
View Journal | View Issue



Cite this: CrystEngComm, 2023, 25, 5842

Improving oxygen reduction reaction and oxygen evolution reaction activities with Ru-NiCo nanoparticles decorated on porous nitrogen-doped carbon for rechargeable Zn-air batteries and OER electrocatalysts†

Lili Sui, b Lihua Miao, b \*a Ye Kuang, Xiaoyan Shen, Dan Yang and He Huang C

The slow kinetics of the oxygen evolution reaction (OER) and oxygen reduction reaction (ORR) in air cathodes severely limit the development of reversible zinc-air batteries. Thus, bifunctional oxygen catalysts with excellent electrocatalytic activity and durability for both the oxygen reduction and oxygen evolution reactions (ORR/OER) are keys to achieving long-term rechargeable zinc-air batteries. However, it remains challenging to further improve the performance by adding more active sites. To address this, a series of nitrogen-doped carbon (CN) with NiCo alloys has been synthesized by pyrolyzing a simple bimetal zeolitic-imidazolate framework (ZIF) and then evenly loaded with metallic Ru nanoparticles, resulting in Ru-NiCo/NC samples. Benefiting from the large pore volume and high activities, the Ru-NiCo/NC electrocatalysts exhibit higher ORR ( $E_{1/2} = 0.84 \text{ V}$ ) and OER performance with an overpotential of 342 mV at 10 mA cm<sup>-2</sup>, along with superior cycle stability. More significantly, when employed in rechargeable zinc-air batteries, Ru-NiCo/NC catalysts demonstrate a high power density of 132.3 mW cm<sup>-2</sup>, significantly outperforming Pt and Ru-based zinc-air batteries. Additionally, DFT (density functional theory) results indicate that the addition of Ru leads to a downshift of the d-band center from the Fermi level, which benefits the reduction of energy barriers and enhances the desorption of O-containing intermediates. This work provides a feasible strategy for developing efficient and high-performance bifunctional electrocatalysts.

Received 11th July 2023, Accepted 8th September 2023

DOI: 10.1039/d3ce00693j

rsc.li/crystengcomm

#### 1. Introduction

With the rapid development of science and technology, human beings face increasingly prominent problems, such as environmental pollution and resource shortage. <sup>1-3</sup> The development of new fine performance and environment-friendly energy materials plays an important role in alleviating energy shortage and promoting national economic development. <sup>4</sup> Among various energy storage systems, as an attractive alternative to traditional lithium-ion batteries, zinc-air batteries have higher energy density and safety, and are promising next-generation batteries. <sup>5,6</sup> However, due to the slow kinetics of the oxygen reduction/reduction reaction

(ORR/OER) and the instability of bifocal catalysts, zinc-air

Currently, Pt based catalysts have high ORR activity, which can speed up reaction kinetics. In practice, however, cost and scarcity are major issues. Therefore, the development of low-cost, highly active alternative materials has become an urgent task. Extensive research has been carried out on transition metal oxides and nonmetallic heteroatom-doped carbon. However, the achievement of a satisfactory ORR is still a challenge. The achievement of a satisfactory of the catalytic activity of metal and nonmetal heteroatoms co-doped with carbon is similar to that of Pt-based catalysts. The mechanism is probably due to an increase in the number of active sites. These results show that transition metal heteroatom doped carbon has potential for developing efficient and low-cost ORR catalysts. However, the reported OER properties of carbon

batteries have great energy loss and poor cycling performance. Thus, highly effective ORR catalysts are essential for energy transformation devices like fuel cells and metal-air batteries.<sup>7,8</sup> In addition, the design of an efficient, affordable, and sustainable dual-function catalyst is very crucial for secondary Zn-air cells.

<sup>&</sup>lt;sup>a</sup> School of Medical Information Engineering, Shenyang Medical College, Shenyang 110043, Liaoning, China. E-mail: ambitious1972@163.com

<sup>&</sup>lt;sup>b</sup> School of pharmacy, Shenyang Medical College, Shenyang, 110043, Liaoning, China

<sup>&</sup>lt;sup>c</sup> Shenyang Ligong University, School of Renewable Energy, Shenyang 110136, P. R. China

<sup>†</sup> Electronic supplementary information (ESI) available. See DOI: https://doi.org/ 10.1039/d3ce00693j

materials are usually not very good. But, the performance of ORR and OER catalysts can be effectively improved by the supported electrocatalysis strategy. Recently, transition metalbased (TM) species/carbon catalysts have attracted wide interest in Zn-air batteries on account of their moderate catalytic property for the ORR/OER. 16,17 Among various composites, zeolitic imidazolate framework (ZIF) derivatives are promising candidates for multi-functional electrocatalysts since these derivate TM-based phases/porous NC composites, which are in situ formed by the conversion of N-containing organic ligands and metal centers in ZIFs, can efficiently catalyze the reversible reactions in Zn-air cells. 18 Nevertheless, it should be noted that the significantly reduced porous channels and aggregated TMbased particles over the high-temperature calcining process will seriously deteriorate the catalytic activity of ZIF-derived catalysts especially for the OER.19 On the other hand, Ru and Ir containing materials have been proved to be superior electrocatalysts for the OER. Therefore, coating Ru or Ir on the ZIF-derived materials with enough pores and highly dispersed TM-based nanoparticles should be a highly desirable procedure to construct ideal bifunctional catalysts. In addition, transition metals are commonly used in combination with other materials, with nickel being a particularly versatile element.<sup>20</sup> NiCo alloys have been shown to exhibit superior activity and decay resistance compared to their single-metal counterparts.21 The bonding between different metals in these alloys can also create intrinsic polarity, thereby enhancing catalytic reactions. Moreover, nickel is known to effectively increase the graphitization degree of carbon materials. 22,23 In addition, the central metal atom is usually the ORR active site. Therefore, the selection of highly active core metal atoms is the most effective strategy to enhance catalytic activity. This is mainly due to the interaction of the d orbital of the central metal atom with the p electrons of oxygen atoms and oxygen-containing intermediates during the ORR process, which leads to the adsorption and subsequent electron transfer of oxygen molecules.<sup>24</sup> Therefore, the chemical properties of the core metal atoms will largely determine the ORR reactivity. Thus, electrocatalysts that incorporate Ru-decorated NiCo/NC can significantly improve the electrocatalytic performance for both the oxygen evolution

Herein, we designed novel Ru decorated NiCo/CN catalysts by a facile pyrolysis strategy. Due to the significantly increased Co and Ni content on the surface of the material, the large number of alloys creates favorable conditions for the formation of active sites and better spatial isolation characteristics. Then, the introduction of Ru speeds up the reaction kinetics and improves the electrocatalytic performance of the material. Ru–NiCo/NC electrocatalysts show higher ORR ( $E_{1/2}=0.84~\rm V$ ) and OER performance with an overpotential of 342 mV at 10 mA cm $^{-2}$  and superior cycle stability. More significantly, the Ru–NiCo/NC catalysts employed in a rechargeable ZAB display a high power density of 132.3 mW cm $^{-2}$  and long cycle stability. DFT results indicate that the addition of Ru can lead to the downshift of the d-band center from the Fermi level, which could be

and reduction reactions (OER and ORR, respectively).

beneficial to reducing energy barriers and boosting the desorption of O-containing intermediates.

#### 2. Results and discussion

The morphology and structural characteristics of the prepared samples were characterized by SEM and TEM. Fig. 1a shows the TEM image. It is found that the NiCo nanoparticles are encapsulated in carbon tubes. This feature was further confirmed by high resolution TEM (Fig. 1b). Simultaneously, the interplanar spacing of 0.176 nm corresponds to the (200) plane of NiCo alloys. Fig. 1c shows the microstructure of the Ru-NiCo/NC nanostructures. It's made up of a lot of curved nanotubes. The metal particles are encapsulated in the nanotubes, and there are no particles on the outside of the nanotubes. The TEM image of the Ru-NiCo/CN catalyst is shown in Fig. 1d. It consists of N-doped graphitic carbon with multilayer ultrathin nanotubes and alloy nanoparticle enrichment zones. Lines are seen around the alloy particles, indicating that the alloy is encased within. The space confinement is especially important in suppressing particle dissolution, which is beneficial for maintaining high stability in the ORR/OER process. Fig. 1(e and f) exhibit the corresponding HRTEM images. The lattice spacing of 0.179 nm can be ascribed to the (200) plane. In addition, the lattice spacing of 3.29 nm can be indexed to the (200) plane of the graphitic carbon phase. By comparing the HRTEM diagram of the two samples, it can be found that the crystal plane spacing of the prepared samples increases significantly after Ru modification. Fig. 1g presents the element distribution mappings of the Ru-NiCo/CN samples. It can be found that Ru, Co, Ni, C and N elements are uniformly distributed throughout the sample. The rich area of the alloy is mainly composed of Co, Ni and N, indicating that there may be a large number of bonds between the alloy and N.

The crystal structures of Ru-NiCo-MOF and the all samples were characterized by XRD. As shown in Fig. 2a and S1,† the characteristic diffraction peak at 26.3° can be indexed to the (002) planes of graphitic carbon. The diffraction peaks at 44.5°, 51.8° and 76.3° belong to the (111), (200), and (220) planes of Ni (JCPDS 04-0850). The other diffraction peaks can be indexed to the (111), (200), and (220) crystal planes of the Co phase (JCPDS 15-0806). The diffraction peak positions of NiCo are in agreement with the NiCo alloys obtained by Mehmood et al.25 No other diffraction peaks can be observed, indicating that the prepared sample possesses high purity and excellent crystallinity. In addition, the absence of Ru indicates that the Ru content in Ru-NiCo/NC is too low to be detected by XRD, or that they are not converted into a new phase, but are present as dopants in the catalyst. The distribution of elements and the valence states of surface elements of the prepared samples were analyzed by XPS. As shown in Fig. 2b, the Co 2p spectra of the two catalysts can be well deconvoluted into four kinds of peaks: metallic Co, Co-N, Co<sup>2+</sup> and satellite peaks. The binding energies at around

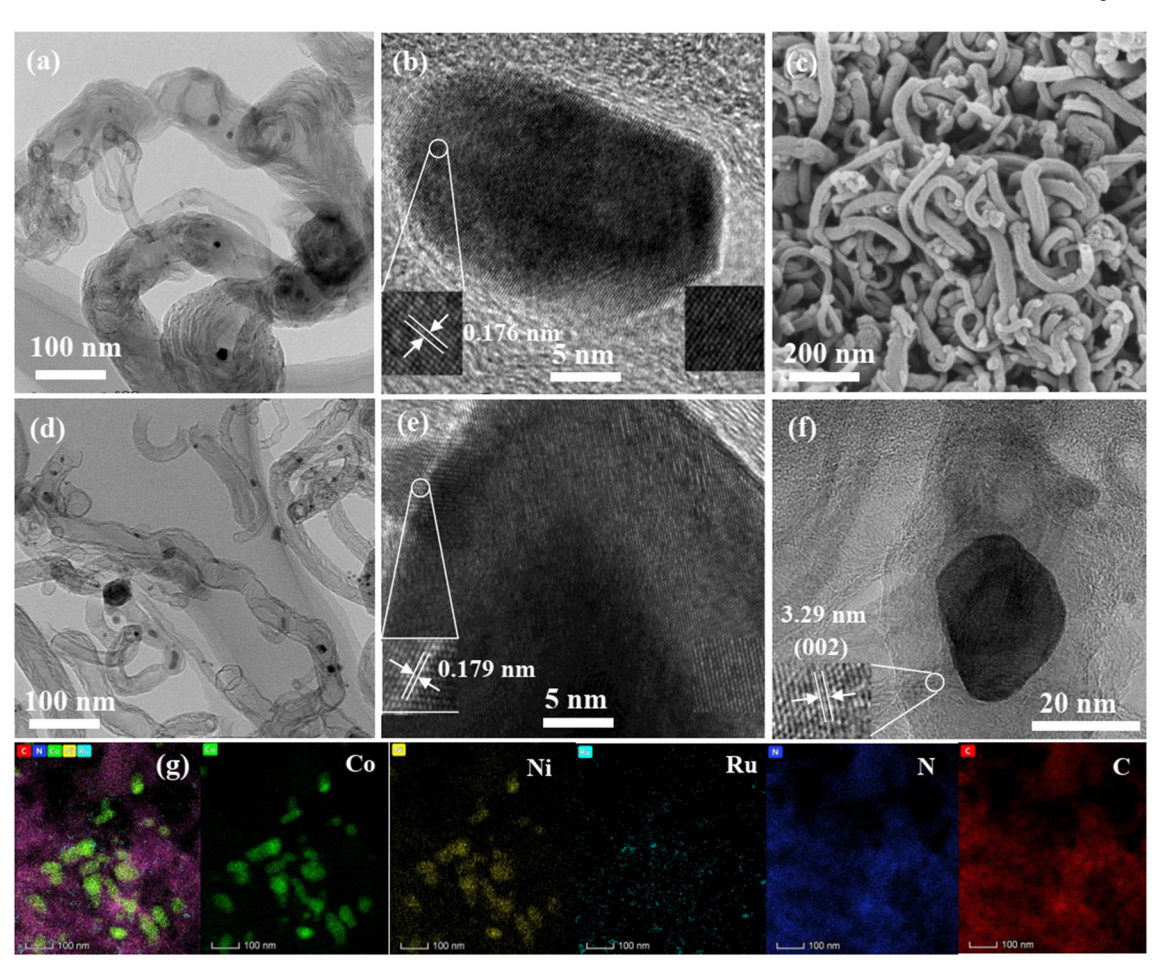


Fig. 1 (a and b) TEM and HRTEM images of NiCo/NC, (c) SEM image of the Ru-NiCo/NC catalyst. (d-f) TEM and HRTEM images of Ru-NiCo/NC. (g) Elemental mappings.

777.8 eV and 793.1 eV can be indexed to metallic Co.26 The peaks at 780.2 eV and 795.2 eV could be ascribed to Co<sup>2+</sup>.27 The peaks at around 782.9 eV and 798.3 eV correspond to Co-N bonds. This reveals that CoN<sub>x</sub> possesses a high proportion, indicating that the surface of the material possesses more active sites. The binding energy of Co 2p in the samples from NiCo/NC to Ru-NiCo/NC moves to the higher energy level region, indicating the formation of strong chemical bonds. The increase of the energy level is beneficial to the enhancement of electrocatalytic performance.<sup>27</sup> The high-resolution Ni 2p spectra (Fig. 2c) show two peaks at around 852.7 and 870.0 eV, which correspond to zero-valence state metallic Ni.28 The relatively weak peaks at binding energies of 855.8 and 873.6 eV can be ascribed to Ni<sup>2+</sup> 2p<sub>3/2</sub> and Ni2+ 2p1/2, respectively, due to the partial oxidation of the sample exposed to air.29 In the high-resolution N 1s spectra (Fig. 2d), the four well-fitted peaks can be indexed to pyridinic-N (404.8 eV), pyrrolic-N (398.6 eV), graphitic-N (401.1 eV), and oxidized-N (401.8 eV), respectively.<sup>30</sup> The successful incorporation of nitrogen atoms into the Ru-NiCo/ NC sample leads to the modulation of the local electronic structure. This enhances the electrical conductivity and creates abundant defects/vacancies, which are favorable for

improving the electrocatalytic performance. The highresolution C 1s spectra (Fig. 2e) can be well fitted into three peaks located at 284.4, 285.3, and 289.1 eV, which are assigned to C-C, C-N, and C-O, respectively.<sup>31</sup> As depicted in Fig. 2f, the deconvoluted Ru 3p peaks show binding energies at 461.6 and 483.2 eV assigned to Ru  $3p_{3/2}$  and Ru  $3p_{1/2}$ . Fig. 2g exhibits the full spectra of the Ru-NiCo/NC and NiCo/ NC samples, confirming the existence of the Ru, Ni, Co, N and C elements. Raman spectra of the all products are measured, as shown in Fig. 2h. The peak located at 1353 cm<sup>-1</sup> can be indexed to the D band, which shows the structural defects and disorder of carbon. The Raman peak at 1591 cm<sup>-1</sup> can be ascribed to the G band, which originates from the disorder-induced C=C vibration and tangential  $E_{2g}$ sp<sup>2</sup> bonded C-C stretching vibration, respectively.<sup>34</sup> The integrated intensity ratio of the D peak to the G peak  $(I_D/I_G)$ , which represents the degree of disorder, can be calculated from the Raman spectra. The results verify that the  $I_{\rm D}/I_{\rm G}$ value of Ru-NiCo/NC is 0.97, which is higher than those of Ru-Co/NC (0.94), Ru-Ni/NC (0.95), NiCo/NC (0.96), Ni/NC (0.93) and Co/NC (0.91). This suggests that the addition of the Ru element leads to an increase in the degree of graphitization. The isothermal nitrogen adsorption-

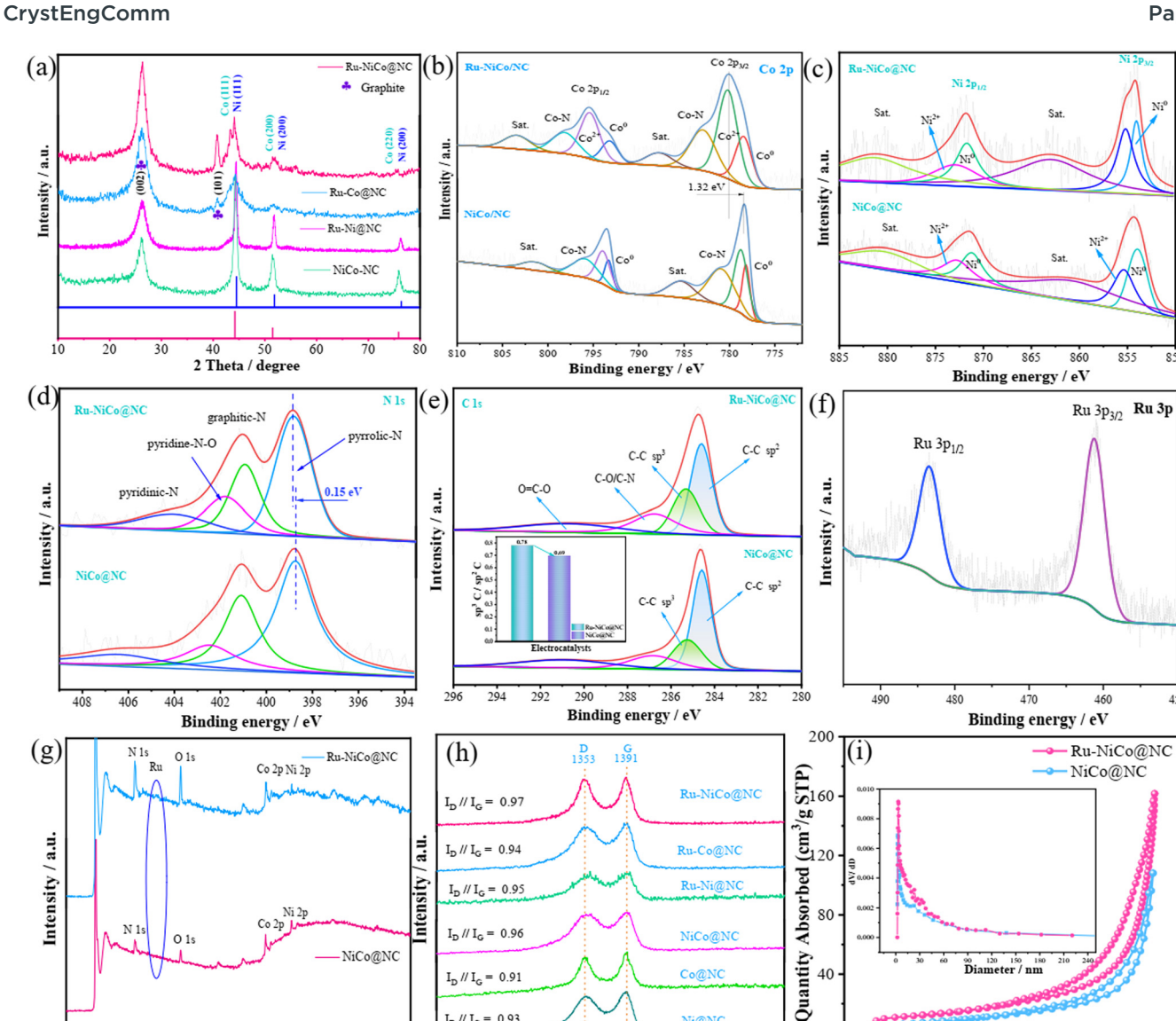


Fig. 2 (a) XRD and (b-q) XPS spectra of the as-prepared samples: (b) Co 2p, (c) Ni 2p, (d) N 1s, (e) C 1s, and (f) Ru 3p, (g) full XPS spectra, (h) Raman spectra, and (i) N<sub>2</sub> adsorption-desorption isotherms, the illustration shows the corresponding aperture distribution curves

Raman shift / cm<sup>-1</sup>

desorption curves are evaluated in Fig. 2i. The IV type hysteresis loops appear in the relative pressure range of 0-1.0, indicating the existence of mesopores.35 In comparison, the Ru-NiCo/NC catalyst shows a BET surface area of 84.6 m<sup>2</sup> g<sup>-1</sup>, which is higher than that of NiCo/NC (58.9 m<sup>2</sup> g<sup>-1</sup>). The inset shows the pore size distribution of the samples, and the Ru-NiCo/NC sample possesses a total pore volume of 18 cm<sup>3</sup> g<sup>-1</sup>. The corresponding average aperture is 2.5 nm. It is found that the Ru-NiCo/NC electrode material presents the largest pore volume and a large number of mesopores, which could lead to the increased oxygen adsorption ability and the availability of active sites.

1000

Binding energy / eV

The OER performance of the as-prepared catalysts is investigated under a three-electrode system in 1 M KOH aqueous solution. All LSV curves of the samples were

obtained with IR compensation at 2 mV s<sup>-1</sup> for the OER. Fig. 3a shows the LSV curves of the as-prepared catalysts. It is found that Ru-NiCo/NC delivers a low overpotential of 342 mV at a current density of 10 mA cm<sup>-2</sup>, which is lower than those of Ru-Co/NC (361 mV), NiCo/NC (398 mV), Co/NC (413 mV), Ru-Ni/NC (437 mV) and Ni/NC (458 mV), and the results showed that Ru modification could significantly improve the electrocatalytic performance of the materials. Meanwhile, it can be found that Co plays a major role in NiCo bimetallic electrocatalysts. The reaction kinetics of the electrocatalysts for the OER can be further analyzed from the Tafel slope, as shown in Fig. 3b. Ru-NiCo/NC exhibits the lowest Tafel slope of 65.75 mV dec<sup>-1</sup>, which is smaller than those of Ru-Co/NC (65.83 mV dec<sup>-1</sup>), NiCo/NC (67.99 mV dec<sup>-1</sup>), Co/NC (69.78 mV dec<sup>-1</sup>), Ru-Ni/NC (129.94 mV dec<sup>-1</sup>)

0.0

0.2

0.6

Relative pressure (P/P<sub>o</sub>)

**Paper** 

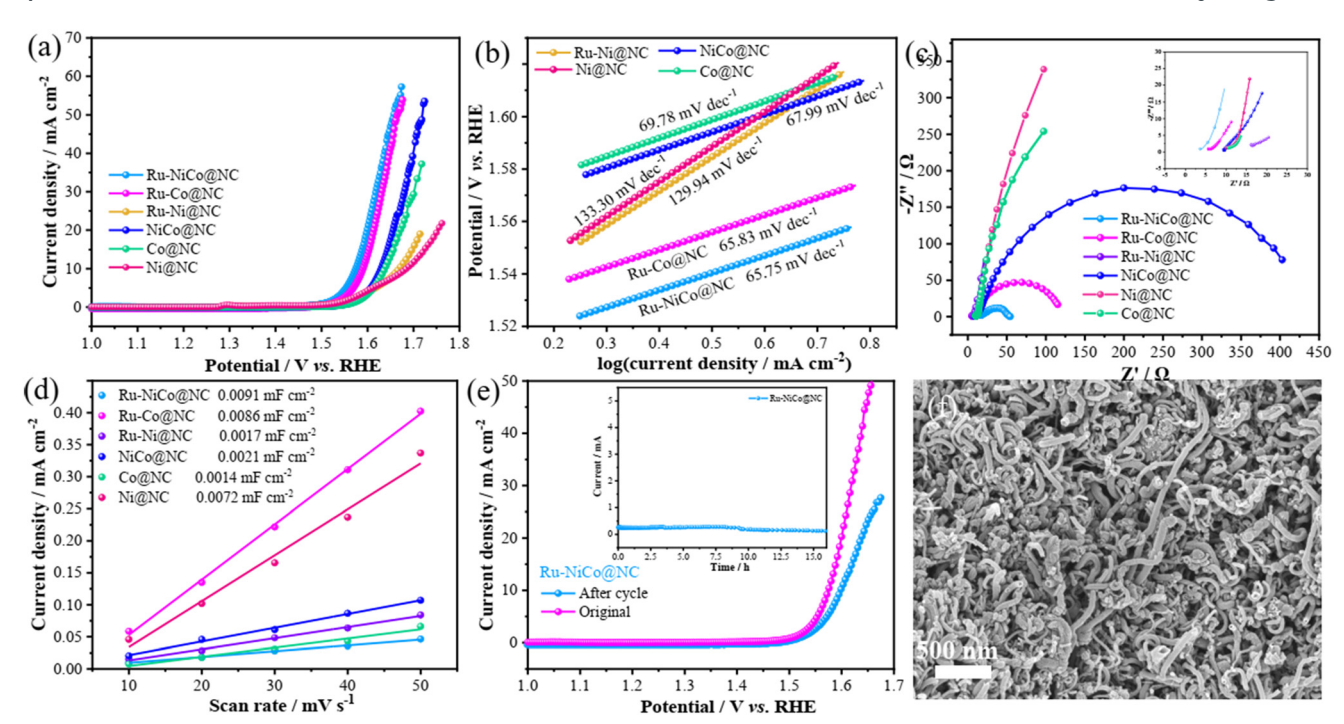


Fig. 3 Electrochemical performances of the catalysts. (a) LSV curves, (b) Tafel slopes, (c) impedance spectra, (d) double-layered capacitance linear fitting, (e) cycle stability, and (f) SEM image after cycling.

and Ni/NC (133.30 mV dec<sup>-1</sup>), indicating that the Ru element decoration can effectively improve the electrocatalytic reaction kinetics. Fig. 3c shows the impedance spectra of the prepared materials. It can be seen from the inset that Ru-NiCo/NC presents a low equivalent resistance (3.7  $\Omega$ ). It is confirmed that Ru-NiCo/NC has the best electrocatalytic performance compared with other materials. To further investigate the intrinsic activity of all electrocatalysts, the electrochemically active surface area (ECSA) is obtained using the electrochemical double-layer capacitance ( $C_{\rm dl}$ ), which can be obtained through fitting the CV curve at different scan rates in the non-faradaic region, as shown in Fig. S1.† It shows that the shapes of all the curves are rectangular, meaning that they belong to the non-faradaic region. Fig. 3d shows the corresponding values of the electrochemical double-layer capacitance. The as-obtained Ru-NiCo/NC catalyst displays the largest ECSA value of 0.0091 mF cm<sup>-2</sup>, which is higher than those of Ru-Co/NC (0.0086 mF cm<sup>-2</sup>), NiCo/NC  $(0.0021 \text{ mF cm}^{-2})$ , Co/NC  $(0.0014 \text{ mF cm}^{-2})$ , Ru-Ni/NC  $(0.0017 \text{ mF cm}^{-2})$  and Ni/NC  $(0.0072 \text{ mF cm}^{-2})$ . This can be attributed to the addition of metal Ru, increasing the active sites of the electrode materials. Fig. 3e shows the cyclic stability test of the Ru-NiCo/NC electrocatalyst. It can be seen from the curve that the performance of the prepared material does not decrease significantly after cycling, which proves that it possesses many active sites and excellent structural stability. It is further confirmed from the illustration that the prepared catalyst still has good cyclic stability after 16 h. Fig. 3f shows the SEM image after cycling. Compared with the SEM image before cycling, it can be found that the material morphology is well maintained.

The ORR performance of the prepared sample was initially evaluated through CV curves. The recorded CV curves of the sample under nitrogen and oxygen conditions are shown in Fig. S2.† It can be observed that the prepared material does not exhibit any oxidation-reduction peaks when saturated with N2, while a significant reduction peak is observed for the prepared catalyst in an O2 atmosphere. This confirms that the prepared material exhibits ORR activity.36,37 The electrocatalytic performance of the prepared samples was then evaluated by LSV. As shown in Fig. 4a, the LSV curves exhibit that the Ru-NiCo/NC catalyst has the best oxygen reduction activity with a positive  $E_{\rm onset}$  of 0.92 V, which is higher than those of Ru-Co/NC (0.91 V), NiCo/NC (0.90 V), Ru-Ni/NC (0.87 V), and Ni/NC (0.83 V). At the same time, Pt/C shows an  $E_{\rm onset}$  of 0.95 V and half-wave potential of 0.86 V. The Ru-NiCo/CN samples present the positively shift halfwave potential (0.84 V) and a higher limiting current density (5.68 mA cm<sup>-2</sup>) than those of Ru-Co/NC (0.83 V@4.98 mA cm<sup>-2</sup>), NiCo/NC (0.82 V@3.92 mA cm<sup>-2</sup>), Ru-Ni/NC (0.76  $V@4.58 \text{ mA cm}^{-2}$ ), Ni/NC (0.80  $V@2.49 \text{ mA cm}^{-2}$ ). In order to further evaluate the reaction kinetics of the prepared catalyst, the corresponding Tafel slope is calculated, as presented in Fig. 4b. Ru-NiCo/NC possesses a low Tafel slope of 38.18 mV dec<sup>-1</sup>, which is smaller than those of Ru-Co/NC (54.20 mV dec<sup>-1</sup>), Ru-Ni/NC (38.48 mV dec<sup>-1</sup>), NiCo/NC (38.4 mV dec<sup>-1</sup>), Co/NC (38.4 mV dec<sup>-1</sup>) and Ni/NC (60.1 mV dec<sup>-1</sup>). The low Tafel slope demonstrates that Ru decoration can increase the ORR reaction kinetics. The electron transfer number of Ru-NiCo/NC was also evaluated through the LSV curves at different rotation rates ranging from 100 to 2500 rpm (Fig. 4c) according to the Koutecky-Levich (K-L) equation.<sup>38</sup>

CrystEngComm Paper

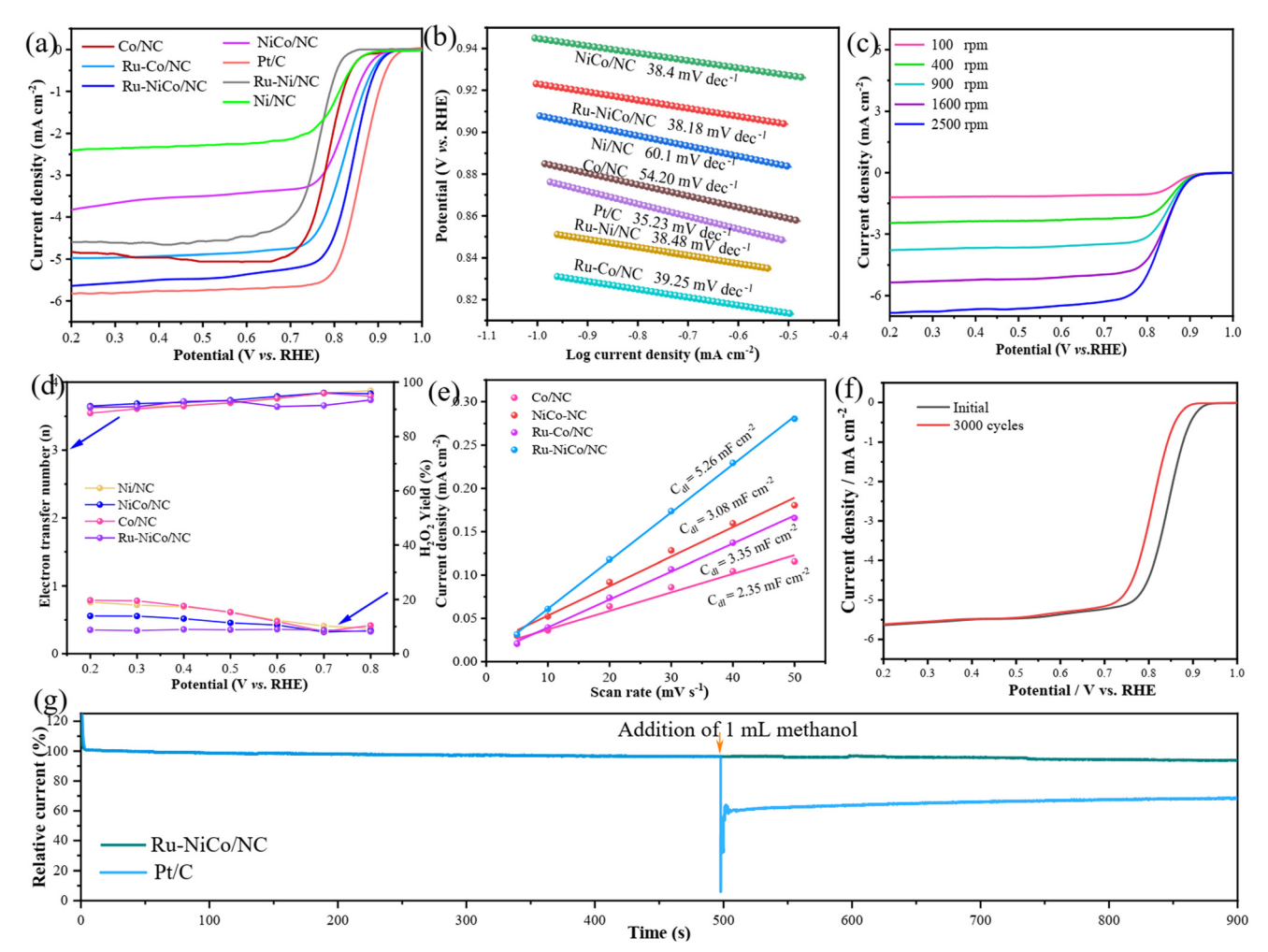


Fig. 4 Electrochemical performances of all catalysts. (a) LSV curves, (b) Tafel slopes, (c) LSV curves of the Ru-NiCo/NC sample and corresponding Koutecky-Levich plots, (d) electron-transfer number and H2O2 yield, (e) double-layered capacitance linear fitting, (f) LSV curves of the Ru-NiCo/NC material before and after 3000 cycles, and (g) chronoamperometric response of Ru-NiCo/NC and Pt/C upon addition of 1 mL methanol.

The n value of the as-obtained samples is 3.92. The n and H<sub>2</sub>O<sub>2</sub> yield were further evaluated using a rotating ring-disk electrode (RRDE, Fig. 4d). The as-prepared material undergoes an obvious four-electron transfer process with nclose to 4 and a H<sub>2</sub>O<sub>2</sub> yield of about 17%. The electrochemically active surface area (ECSA) is obtained from the double-layer capacitance, and it can be calculated from the CV curves in the non-faradaic region. In Fig. 4e, the Ru-NiCo/NC catalyst shows a high  $C_{\rm dl}$  value of 5.26 mF cm<sup>-2</sup>, which is higher than those of Ru-Co/NC (3.35 mF cm<sup>-2</sup>), NiCo/NC (3.08 mF cm<sup>-2</sup>) and Co/NC (2.35 mF cm<sup>-2</sup>). The results show that Ru can improve the specific activity of the electrocatalysts. Cyclic stability is an important evaluation factor, as shown in Fig. 4f. The  $E_{1/2}$  of the Ru-NiCo/NC catalyst presents a low decay of 28 mV after 3000 cycles, revealing that the Ru-NiCo/NC material possesses excellent cycle stability. In addition, Ru-NiCo/NC exhibits compelling methanol tolerance after injecting methanol into the electrolyte (Fig. 4g). It is obviously superior to commercial Pt/C electrode materials.

Through the above performance test and structural characterization, it can be found that the prepared catalyst shows an excellent electrochemical performance. In order to further explore its practical application, the corresponding zinc-air battery was assembled. Zinc-air batteries have attracted wide attention owing to their high specific energy density. As shown in Fig. 5a and g, the as-obtained Ru-NiCo/ NC catalyst was used as the air cathode for the zinc-air batteries, a Zn plate was selected as the anode material and a 6.0 M KOH + 0.2 M Zn(Ac)<sub>2</sub> solution as the electrolyte. The assembled Ru-NiCo/NC device exhibits an open-circuit voltage of 1.44 V (Fig. 5b), which is higher than that of commercial Pt/C-RuO2. Fig. 5c presents the GCD curves of the device. The zinc-air battery with the Ru-NiCo/NC cathode catalyst delivers a peak power density of 132.3 mW cm<sup>-2</sup>, which is higher than that of Pt/C-RuO<sub>2</sub> (41.2 mW cm<sup>-2</sup>). In addition, the zinc-air battery with the Ru-NiCo/NC cathode shows a discharge specific capacity of 767.9 mA h g<sup>-1</sup> at 10 mA cm<sup>-2</sup>, which is higher than that of Pt/C (658.6 mA h g<sup>-1</sup>) (Fig. 5e). It can be seen from Fig. 5f that the two devices can

**Paper** 

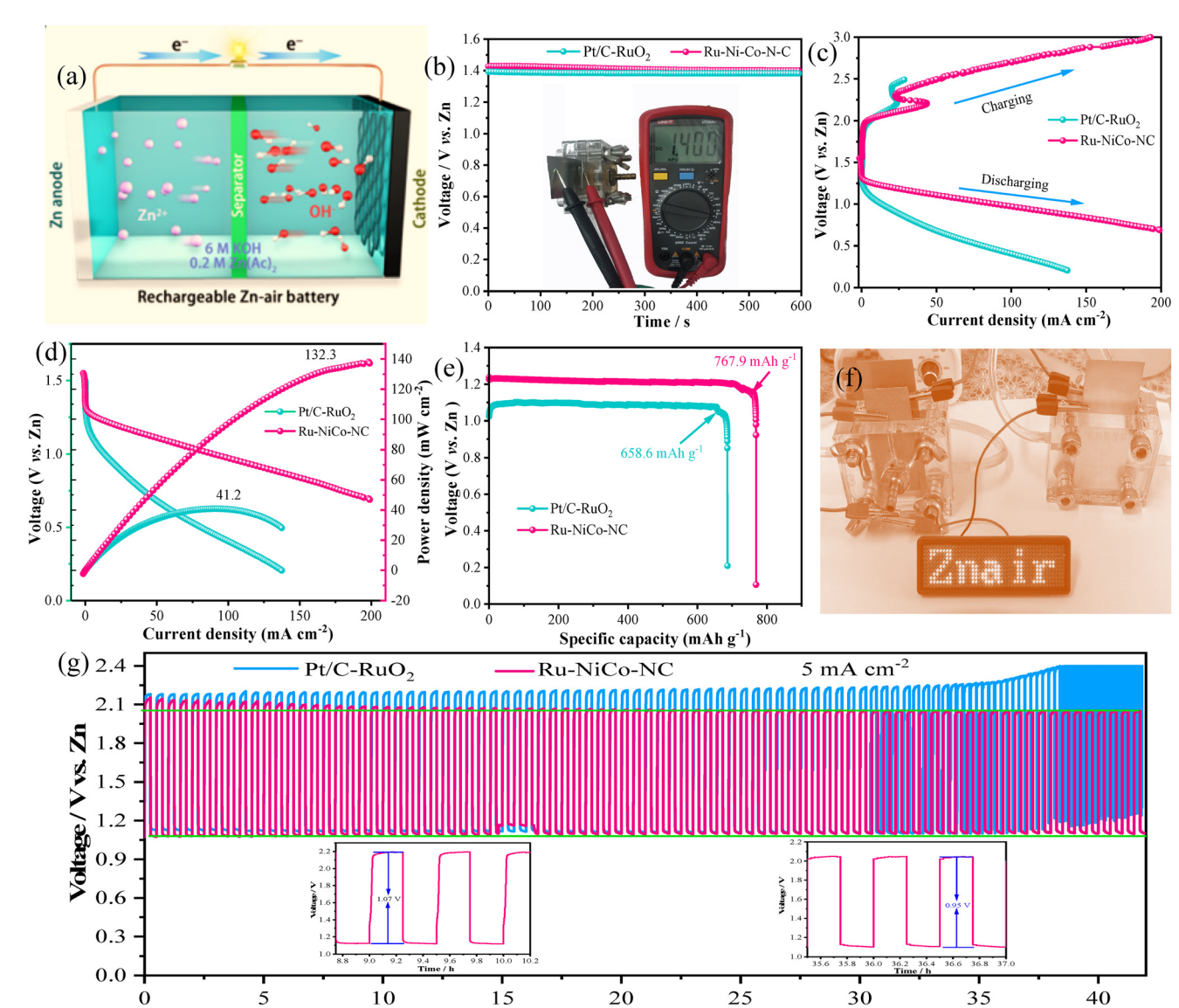


Fig. 5 (a) Schematic illustration of an aqueous ZAB, (b) digital photograph showing an open-circuit potential of 1.4 V, (c) charge and discharge polarization curves, (d) power densities, (e) specific capacities of the zinc-air battery, (f) image of the assembled device and (g) galvanostatic charge-discharge cycle curves of aqueous ZABs, inset shows the charge and discharge curves of the front and back turns.

Time / h

power a display. When the zinc-air battery with the Ru-NiCo/NC cathode was galvanostatically discharged at a current density of 10 mA cm<sup>-2</sup> for more than 45 h, it is found that the discharge voltage is 1.07 V. The voltage decreases to 0.95 V after 45 h cycling. The results show that the prepared material exhibits excellent cycle stability (Fig. 5g and inset).

DFT calculations are employed to further understand the mechanism of Ru decoration for enhancing electrocatalytic performance. Fig. 6a and b depict the theoretical models of the NiCo/NC and Ru–NiCo/NC samples. The bonding and antibonding states of covalent bonds were characterized by the crystal orbital Hamilton population (COHP) method, as shown in Fig. 6c and d. The COHP values of Co–N and N–C bonds of the Ru–NiCo/NC material are –10.53 and –2.89, respectively, and are lower than those of the NiCo/NC

product (-0.102 and -0.002). This suggests that Ru modification can improve the antibonding state near the Fermi level and that Co-N interactions are more stable and stronger than C-N bonds. Thus, the filling of antibonding states is reduced and the adsorption of H<sub>2</sub>O\* is enhanced. The density of states (DOS) of the electrocatalysts is calculated and presented in Fig. 6(d and e). The analysis shows that the addition of Ru significantly increases the energy near the Fermi level, and the d band center decreases from -3.97 eV to -1.49 eV. The results show that Ru modification can significantly improve the electrical conductivity and optimize the distribution characteristics of the electronic structure. Then, we further studied the reaction energy changes caused by the introduction of Ru, as presented in Fig. 6g. By comparing the adsorption energy

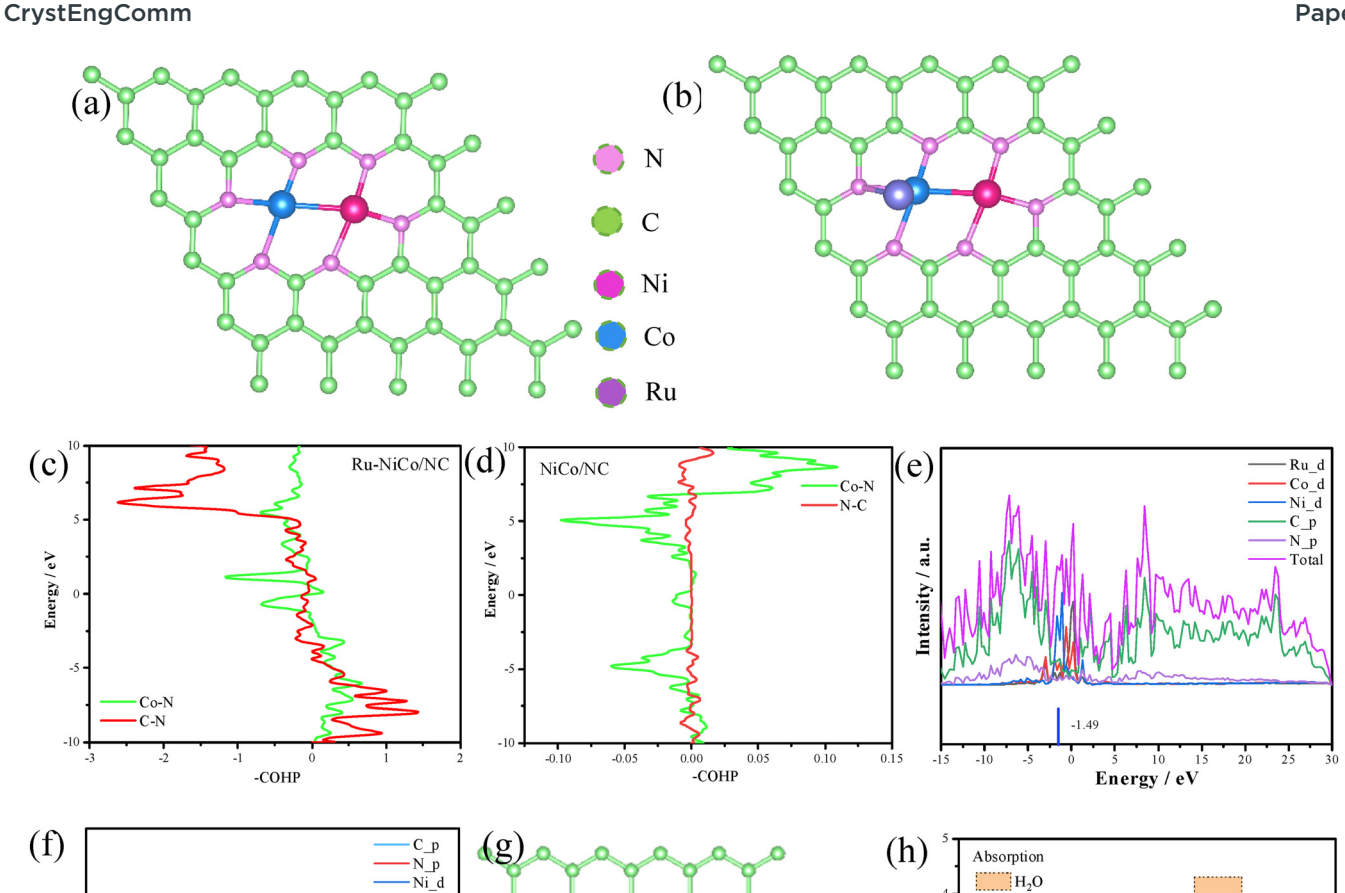


Fig. 6 Crystalline models of (a) NiCo/NC and (b) Ru-NiCo/NC, (c and d) COHP of Ru-NiCo/NC and NiCo/NC, (e) pDOS of Ru-NiCo/NC, (f) pDOS of the NiCo/NC sample, (g) model of Ru-NiCo/NC with adsorbed H<sub>2</sub>O, and (h) adsorption energies for O<sub>2</sub> and H<sub>2</sub>O.

of the Ru modified samples, it can be found that the Ru-NiCo/NC electrocatalyst exhibits strong adsorption of O<sub>2</sub> and H<sub>2</sub>O, and the corresponding adsorption energies (Fig. 6h) of the Ru-NiCo/NC electrocatalyst are -0.06 eV and 4.30 eV, respectively. Its performance is better than that of the NiCo/NC electrocatalyst. The results show that the Ru-NiCo/NC electrocatalyst exhibits excellent OER and ORR performance.

Energy / eV

## 3. Conclusion

Intensity / a.u.

In summary, we designed novel Ru decorated NiCo/CN catalysts by a facile pyrolysis strategy. Due to the significantly increased Co and Ni content on the surface of the material, the large number of alloys creates favorable conditions for the formation of active sites and better spatial isolation characteristics. Meanwhile, the alloys greatly enhanced the specific surface area and degree of graphitization of the overall material. Then, the introduction of Ru speeds up the kinetics and improves the electrocatalytic performance of the material. The Ru-NiCo/NC electrocatalyst shows higher ORR ( $E_{1/2} = 0.84 \text{ V}$ ) and OER performance with an overpotential of 342 mV at 10 mA cm<sup>-2</sup> and superior cycle stability. More significantly, the Ru-NiCo/NC catalyst employed in rechargeable Zn-air batteries displays a high power density of 132.3 mW cm<sup>-2</sup> and long cycle stability. DFT calculations show that the addition of Ru can enhance the electroactivity of the active sites. This not only increases the binding strength of the key intermediates but also reduces the overpotential of the ORR. Thus, this work provides an effective paradigm for improving catalytic kinetics and activity through noble metal modification, thereby introducing desired functionality, which may be easily extended to the design of other highly efficient catalysts.

O<sub>2</sub>

Inergy / eV

Ru-NiCo/NC

Paper CrystEngComm

## Conflicts of interest

The authors declare no conflict of interest.

#### **Acknowledgements**

This project is supported by the Education Department of Liaoning Province (LJKMZ20221794) and the Innovative training program for college students (S202310164016).

#### References

- 1 T. T. Wang, W. H. Zeng, J. W. Zhu, W. X. Tian, J. Wang, J. S. Tian, D. C. Yuan, S. J. Zhang and S. C. Mu, Nano Energy, 2023, 113, 108577.
- 2 X. Y. Gu, M. Yu, S. Q. Chen, X. Q. Mu, Z. H. Xu, W. Q. Shao, J. J. Zhu, C. Y. Chen, S. L. Liu and S. C. Mu, Nano Energy, 2022, 102, 107656.
- 3 D. Feng, P. Y. Wang, R. Qin, W. J. Shi, L. Gong, J. W. Zhu, Q. L. Ma, L. Chen, J. Yu, S. L. Liu and S. C. Mu, Adv. Sci., 2023, 10, 2300342.
- 4 F. T. Fu, Y. F. Chen, Z. M. Cui, Y. T. Li, W. D. Zhou, S. Xin, Y. W. Tang and J. B. Goodenough, Nano Lett., 2016, 16, 6516-6522.
- 5 X. Luo, X. Tan, P. X. Ji, L. Chen, J. Yu and S. C. Mu, EnergyChem, 2023, 5, 100091.
- 6 Z. J. Li, X. D. Wu, X. Jiang, B. B. Shen, Z. S. Teng, D. M. Sun, G. T. Fu and Y. W. Tang, Adv. Powder Technol., 2022, 1, 100020.
- 7 X. Q. Mu, X. Y. Gu, S. P. Dai, J. B. Chen, Y. J. Cui, Q. Chen, M. Yu, C. Y. Chen, S. L. Liu and S. C. Mu, Energy Environ. Sci., 2022, 15, 4048-4057.
- 8 O. Keisar, Y. Ein-Eli, Y. Alfi and Y. Cohen, J. Power Sources, 2020, 450, 227545.
- 9 S. K. Singh, K. Takeyasu and J. Nakamura, Adv. Mater., 2019, 31, 1804297.
- 10 L. Zhao, Q. Wang, X. Zhang, C. Deng, Z. Li, Y. Lei and Zhu, ACS Appl. Mater. Interfaces, 2018, 35888-35895.
- 11 J. F. Kong and W. L. Cheng, Chin. J. Catal., 2017, 38, 951-969.
- 12 J. Tan, X. He, F. Yin, B. Chen, G. Li, X. Liang and H. Yin, Catal. Today, 2021, 364, 67.
- 13 D. Chen, R. H. Yu, D. L. Wu, H. Y. Zhao, P. Y. Wang, J. W. Zhu, P. X. Ji, Z. H. Pu, L. Chen, J. Yu and S. C. Mu, Nano Energy, 2022, 100, 107445.
- 14 S. Huang, Y. Meng, Y. Cao, S. He, X. Li, S. Tong and M. Wu, Appl. Catal., B, 2019, 248, 239-248.
- 15 Y. Peng, Y. Bai, C. Liu, S. Cao, Q. Kong and H. Pang, Coord. Chem. Rev., 2022, 466, 214602.
- 16 L. Yang, H. Xu, H. Liu, X. Zeng, D. Cheng, Y. Huang, L. Zheng, R. Cao and D. Cao, Research, 2020, 9, 7593023.

- 17 P. Rao, Y. Liu, Y.-Q. Su, M. Zhong, K. Zhang, J. Luo, J. Li, C. Jia, Y. Shen, C. Shen and X. Tian, Chem. Eng. J., 2021, 422,
- 18 X. Wang, J. Wang, P. Wang, L. Li, X. Zhang, D. Sun, Y. Li, Y. Tang, Y. Wang and G. Fu, Adv. Mater., 2022, 34, 2206540.
- 19 H. Jiang, Y. Liu, W. Li and J. Li, Small, 2018, 14, 1703739-1703748.
- 20 X. Zhang, C. Y. Wang, Y. N. Chen, X. G. Wang, Z. J. Xie and Z. Zhou, J. Power Sources, 2018, 377, 136-141.
- 21 Y. X. Zhao, Q. X. Lai, Y. Wang, J. J. Zhu and Y. Y. Liang, ACS Appl. Mater. Interfaces, 2017, 9, 16178-16186.
- 22 B. W. Wang, X. X. Wang, J. X. Zou, Y. C. Yan, S. H. Xie, G. Z. Hu, Y. G. Li and A. G. Dong, Nano Lett., 2017, 17, 2003-2009.
- 23 Z. Li, H. He, H. Cao, S. Sun, W. Diao, D. Gao, P. Lu, S. Zhang, Z. Guo, M. Li, R. Liu, D. Ren, C. Liu, Y. Zhang, Z. Yang, J. Jiang and G. Zhang, Appl. Catal., B, 2019, 240, 112-121.
- 24 W. Z. Cheng, P. F. Yuan, Z. R. Lv, Y. Y. Guo, Y. Y. Qiao, X. Y. Xue, X. Liu, W. L. Bai, K. X. Wang, Q. Xu and J. N. Zhang, Appl. Catal., B, 2020, 260, 118198.
- 25 A. Mukhtar, B. S. Khan and T. Mehmood, Appl. Phys. A: Mater. Sci. Process., 2016, 122, 1022.
- 26 L. Zhong, Q. Huang, J. Y. Ding, Y. Y. Guo, X. Wang, L. L. Chai, T. T. Li, Y. Hu, J. J. Qian and S. M. Huang, J. Power Sources, 2021, 492, 229632.
- 27 X. L. Guo, T. X. Zheng, G. P. Ji, Hu Ni, C. H. Xu and Y. X. Zhang, J. Mater. Chem. A, 2018, 6, 10243-10252.
- 28 L. Yang, L. Shi, D. Wang, Y. Lv and D. Cao, Nano Energy, 2018, 50, 691-698.
- 29 T. R. Zhan, X. L. Liu, S. S. Lu and W. G. Hou, Appl. Catal., B, 2017, 205, 551-558.
- 30 W. Yao, J. M. Chen, Y. J. Wang, R. Q. Fang, Z. Qin, X. F. Yang, L. Y. Chen and Y. W. Li, Angew. Chem., Int. Ed., 2021, 60, 23729-23734.
- 31 T. H. Zhou, Y. H. Du, S. M. Yin, X. Z. Tian, H. B. Yang, X. Wang, B. Liu, H. M. Zheng, S. Z. Qiao and R. Xu, Energy Environ. Sci., 2016, 9, 2563-2570.
- 32 X. Wang, Y. Jia, X. Mao, D. Liu, W. He, J. Li, J. Liu, X. Yan, J. Chen, L. Song, A. Du and X. Yao, Adv. Mater., 2020, 32, 2000966.
- 33 Y. N. Chen, X. Zhang, H. J. Cui, X. Zhang, Z. J. Xie and X. G. Wang, Energy Storage Mater., 2018, 15, 226-233.
- 34 Y. J. Huo, X. Y. Peng, X. J. Liu and J. Luo, ACS Appl. Mater. Interfaces, 2018, 10, 12618-12625.
- 35 L. Xu, Q. Q. Jiang, Z. H. Xiao, X. Y. Li, J. Huo, S. Y. Wang and L. M. Dai, Angew. Chem., 2016, 128, 5363-5367.
- 36 X. Li, L. Liu, X. Ren, J. Gao, Y. Huang and B. Liu, Sci. Adv., 2020, 6, eabb6833.
- 37 B. Q. Li, S. Y. Zhang, X. Chen, C. Y. Chen, Z. J. Xia and Q. Zhang, Adv. Funct. Mater., 2019, 29, 1901301.
- D. J. Yang, L. J. Zhang, X. C. Yan and X. D. Yao, Small Methods, 2017, 1, 1700209.